Research Square

Preprints are preliminary reports that have not undergone peer review.
They should not be considered conclusive, used to inform clinical practice,
or referenced by the media as validated information.

Spatio-temporal Evolution Characteristics and Interrelationships between Land Surface Temperatures and Air Pollutants in Chinese Cities

Yonghe Feng
China University of Mining and Technology
Guie Li
geli@cumt.edu.cn
China University of Mining and Technology
Qingwu Yan
China University of Mining and Technology

Research Article

Keywords: Land surface temperature, Air pollution, Exploratory Spatio-temporal Data Analysis, Multifractal Detrended Cross-Correlation Analysis, Continuous Wavelet Transform

Posted Date: February 26th, 2026

DOI: https://doi.org/10.21203/rs.3.rs-8670452/v1

License: This work is licensed under a Creative Commons Attribution 4.0 International License.
Read Full License

Additional Declarations: No competing interests reported.

Spatio-temporal Evolution Characteristics and Interrelationships between Land Surface Temperatures and Air Pollutants in Chinese Cities

Yonghe Feng · Guie Li(✉) · Qingwu Yan
e-mail: 07223747@cumt.edu.cn · geli@cumt.edu.cn · yanqingwu@cumt.edu.cn
[1]
School of Environment and Spatial Informatics, China University of Mining and Technology, Xuzhou, 221116, China

ARTICLEINFO

Keywords:
Land surface temperature
Air pollution
Exploratory Spatio-temporal Data Analysis
Multifractal Detrended Cross-Correlation Analysis
Continuous Wavelet Transform

ABSTRACT

Urbanization in China has profoundly altered the urban thermal environment and air quality, imposing significant pressures on urban ecosystems. While the urban heat island (UHI) effect and air pollution are often studied in parallel, their spatio-temporal interrelationships remain complex and not fully quantified across different scales. This study investigates the coupling between land surface temperature (LST) – a key driver of UHI – and major air pollutants (PM2.5, PM10, O3) across Chinese cities from 2003 to 2024. We employ a suite of advanced analytical methods, including spatial correlation analysis to characterize the spatial dependence of LST within urban agglomerations, and trajectory modeling to identify key pollution-affected regions and dispersion pathways. Methodologically, the core innovation lies in integrating Continuous Wavelet Transform (CWT), Seasonal-Trend decomposition using Loess (STL), and Multifractal Detrended Cross-Correlation Analysis (MF-DCCA). This integrated framework enables a novel multi-scale analysis that captures both the time-frequency dynamics and seasonal characteristics inherent in the LST-pollutant relationship. Our results reveal distinct scale-dependent associations: The relationship between PM2.5 and LST is relatively straightforward at larger scales, whereas the linkage between O3 and LST exhibits the greatest complexity across scales. Conversely, PM10 shows a clearer association with LST at smaller scales. Notably, the strength of cross-correlations for all three pollutants diminishes at larger scales. The multiscale approach advanced in this study successfully quantifies the multi-faceted interplay between LST and pollutants, effectively overcoming the limitations of conventional spatio-temporal analyses. It establishes a new paradigm for elucidating nonlinear relationships in complex environmental systems and provides an efficient methodology for deepening our understanding of the coupling mechanisms between air pollution and the urban thermal environment.

[1] **Funding**
This research has been supported by the National Natural Science Foundation of China(42101459).Guie Li(✉)geli@cumt.edu.cn

1. Introduction

China's rapid economic growth and urbanization have driven the extensive conversion of natural landscapes to impervious artificial surfaces (Liu et al., 2021), fundamentally reshaping land-use structures (Chen et al., 2021). This transformation reduces surface albedo and increases thermal capacity in urban areas, resulting in systematically higher Land Surface Temperature (LST) in cities compared to their rural surroundings. Elevated urban LST is the fundamental driver of the Urban Heat Island (UHI) effect—a distinct thermal phenomenon with profound implications for climate, energy consumption, ecosystem stability, and public health (Qi et al., 2023; Sabrin et al., 2020; Tesfamariam et al., 2023). Concurrently, intensive human activities such as fossil fuel combustion release substantial amounts of air pollutants, including $PM_{2.5}$, PM_{10}, and O_3 (Kumari et al., 2021). Critically, the thermal environment shaped by high urban LST and the chemical environment laden with pollutants do not exist in isolation; they interact synergistically, exacerbating risks related to climate warming, ecological stress, and human well-being (Friederike et al., 2021). Therefore, understanding the spatiotemporal relationship between LST (as the core thermal metric) and air pollution is essential for developing integrated urban environmental management strategies.

Extensive research confirms a complex interplay between urban thermal and pollution fields. LST patterns influence atmospheric boundary layer dynamics and the transport-diffusion processes of pollutants, thereby affecting their concentration and spatial distribution (Abbassi et al., 2020). Conversely, pollutants can alter radiative energy budgets and cloud microphysics, feeding back on surface temperatures. However, the precise nature and directionality of this relationship remain contested. Some studies report a positive feedback mechanism, where higher LST intensifies pollution episodes, which in turn further elevates surface temperatures (Feizizadeh & Blaschke, 2013). Others suggest that under specific meteorological conditions, urban-rural thermal contrasts may enhance air exchange and promote pollutant dispersion, implying a more complex or even negative correlation in certain contexts (Zhong et al., 2018). Empirical findings further demonstrate significant variability and inconsistency. For example, in the Yangtze River Delta, LST exhibited negative correlations with $PM_{2.5}$ and PM_{10} but a positive correlation with O_3 (Jiang et al., 2023), highlighting that relationships are not only context-dependent but also pollutant-specific. These contradictions underscore the scale-sensitive and non-stationary nature of the LST-pollution nexus, suggesting that interactions may vary across different temporal scales and evolve over time.

Despite growing scholarly interest, three significant research gaps hinder a systematic and mechanistic understanding. First, a predominant focus on the generalized UHI phenomenon or localized case studies has often overshadowed a direct and consistent examination of LST as the primary, quantifiable thermal variable in large-scale, long-term analyses. Second, studies frequently investigate single pollutants or employ aggregated air quality indices, potentially obscuring the distinct and possibly divergent physical and chemical pathways through which LST interacts with different pollutant species. Third, methodological limitations in conventional analytical approaches have constrained the ability to detect and characterize the multi-scale (from seasonal to decadal), nonlinear, and potentially long-memory spatiotemporal dependencies that are hypothesized to govern this complex geophysical coupling.

To address these gaps, this study aims to systematically investigate the spatiotemporal evolution and scale-specific interrelationships between LST and key air pollutants ($PM_{2.5}$, PM_{10}, O_3) across more than 370 Chinese cities from 2003 to 2024. By centering the analysis explicitly on satellite-derived LST—the direct radiative temperature of the urban surface—we move beyond generalized UHI discussions to provide a precise, process-oriented investigation of thermal-pollution coupling. The novelty of this research is twofold: (1) conceptual, through its integrated focus on LST and multiple, distinct pollutants over a national scale and extended timeframe; and (2) methodological, through the innovative integration of a suite of advanced spatiotemporal analytical techniques designed to overcome previous limitations.

This comprehensive analytical framework incorporates the following methods, each selected for its specific capability to address the identified complexities:

Exploratory Spatiotemporal Data Analysis (ESTDA) will be employed to characterize the fundamental spatial patterns, heterogeneity, and dynamic evolution of both LST and pollutant fields. ESTDA techniques, such as spatiotemporal autocorrelation analysis, are crucial for visualizing and statistically confirming the non-random spatial structure and its changes over time, providing the foundational geographic context.

Seasonal-Trend decomposition using Loess (STL) will be applied to decouple the observed time series of each variable into three interpretable components: seasonal, long-term trend, and residual. This decomposition is essential to isolate the underlying secular trends from periodic seasonal cycles and irregular noise, allowing for a clearer analysis of the core, non-cyclic relationship between LST and pollutants.

Continuous Wavelet Transform (CWT) will be used to identify the dominant temporal scales (e.g., intra-annual, inter-annual) of variability inherent in the LST and pollutant series and to examine how these scales of influence change throughout the study period. CWT is particularly powerful for revealing non-stationary periodicities and localized intermittent oscillations that traditional Fourier analysis might miss.

MultiFractal Detrended Cross-Correlation Analysis (MF-DCCA) will be utilized to rigorously quantify the scale-specific, long-range cross-correlations between the LST and each pollutant series. This method is uniquely suited for detecting nonlinear interactions, assessing the strength and persistence of coupling across different time windows (e.g., short-term vs. long-term), and revealing whether their joint behavior exhibits multifractal characteristics, indicative of complex, scale-invariant dynamics.

Through the sequential and complementary application of these methods, this study seeks to: (1) delineate the long-term trends and spatial dynamics of LST and key pollutants across China's urban system; (2) disentangle their seasonal, trend, and irregular components; and (3) quantify their multi-scale, nonlinear interdependencies. The findings are expected to elucidate the dynamic, scale-dependent, and pollutant-specific linkages between the urban thermal landscape and air quality, thereby offering novel empirical insights and a refined analytical framework to inform more effective and coordinated urban heat mitigation and air pollution control strategies.

2. Study area

This study is based on a comprehensive evaluation of data availability and accuracy for both pollutant concentrations and LST. Through systematic screening, more than 370 Chinese cities with complete data records were selected for analysis. Figure 1 illustrates the spatial distribution of these cities against the backdrop of nine major land use/cover types across China.

The research covers the period from 2003 to 2024. This extended timeframe enables a more robust analysis of long-term trends and cyclical fluctuations in the relationship between LST and pollutants. The extended temporal window is crucial for accurately capturing complex, evolving dynamics and is therefore essential for addressing the core research question of this study.

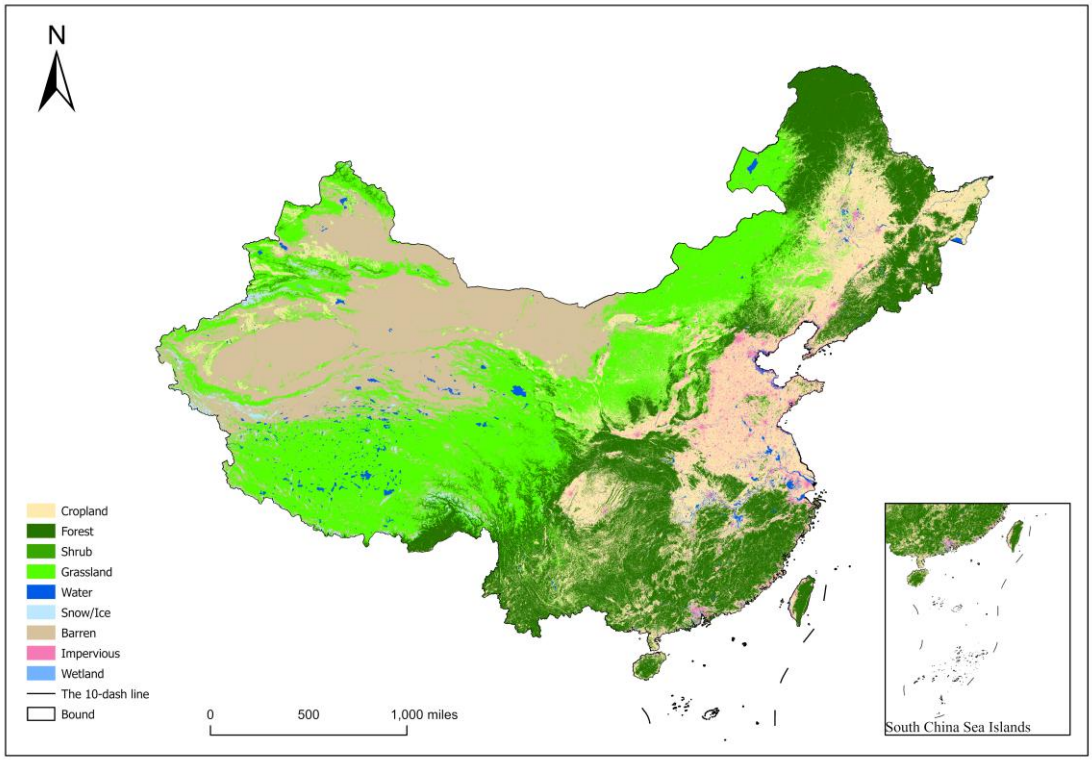


Fig.1. Distribution and Location of Land Cover Types in China

3. Data and methods

3.1 Data

This study is based on two primary datasets: LST data and air pollutant concentration data.

The LST data were sourced from the Terra/MODIS 8-day composite product (MOD11A2), which is a standard Level 3 land product with a spatial resolution of 1 km. The raw data, provided in Hierarchical Data Format-Earth Observing System (HDF-EOS) format, were converted to Kelvin-scale LST values using the standard scaling factor as per the product documentation:

$$\mathrm{LST} = \mathrm{DN} \cdot 0.02 - 273.15 \tag{1}$$

Where DN (Digital Number) is the integer value stored for each pixel. The final LST values in degrees Celsius (°C) were obtained by subtracting 273.15 from the Kelvin values. It is important to note that in the MOD11A2 product, the DN values already represent scaled LST, not top-of-atmosphere brightness temperature (Wan et al., 2015).

Air pollutant data, including ozone (O_3), fine particulate matter ($PM_{2.5}$), and inhalable particulate matter (PM_{10}), span the period from 2003 to 2024. The original monitoring data were obtained from the China National Environmental Monitoring Centre. The monthly and annual mean concentrations were calculated from the daily 24-hour average datasets of Wei et al. (2020, 2021).

Additionally, land use/cover data for the year 2021 were acquired from the China Land Cover Dataset (CLCD), which has a spatial resolution of 30 meters (Yang & Huang, 2022), providing the foundational geographic context for spatial analysis.

3.2 Methods

3.2.1. Spatial autocorrelation analysis

Spatial autocorrelation is a method in spatial analysis that examines the correlation of the same attribute across different spatial units. By assessing both global and local spatial correlations and clustering patterns in the data, it helps reveal the spatial evolution and aggregation characteristics of air pollutants. Global spatial autocorrelation is calculated using Equations (2), (3), and (4).

$$\mathrm{I} = \frac{\mathrm{n}\sum_{i=1}^{\mathrm{n}}\sum_{j=1}^{n} W_{ij}(x_i-\bar{x})(x_j-\bar{x})}{\sum_{i=1}^{\mathrm{n}}\sum_{j=1}^{n} W_{ij}(x_i-\bar{x})^2} = \frac{\sum_{i=1}^{\mathrm{n}}\sum_{j\neq 1}^{n} W_{ij}(x_i-\bar{x})(x_j-\bar{x})}{S^2\sum_{i=1}^{\mathrm{n}}\sum_{j\neq 1}^{n} W_{ij}} \tag{2}$$

$$\mathrm{S}^2 = \frac{\sum_{i=1}^{n}(x_i-\bar{x})^2}{n} \tag{3}$$

$$\mathrm{W_{ij}} = \begin{bmatrix} w_{11} & \cdots & w_{j1} \\ \vdots & \ddots & \vdots \\ w_{i1} & \cdots & w_{in} \end{bmatrix} \tag{4}$$

In the formula, I is the Global Moran's Index.x_i represents the observed value of region i. n represents the total number of observed samples. $\mathrm{W_{ij}}$ represents the spatial weight. $\bar{x}$ is the average value of x.

Global spatial autocorrelation cannot accurately represent specific local spaces that indicate agglomeration or anomalies. In contrast, the Local Indicators of Spatial Autocorrelation (LISA) can reveal the spatial correlation and differential characteristics of pollutants in each study unit, as shown in Eq.(5).

$$\mathrm{I}_i = \frac{(x_i-\bar{x})\sum_j (x_i-\bar{x})}{S^2} \tag{5}$$

For the spatial autocorrelation test, the standardized statistic Z is presented as in Eq.(6):

$$Z(I) = [I - E(I)]/\sqrt{\mathrm{var}(I)} \tag{6}$$

Where $\mathrm{I_i}$ is the local Moran index, E(I) is the expected value, and var(I) represents the coefficient of variation. If the value is positive, it indicates high values clustering with each other or low values clustering. If the value is negative, it indicates that high and low values cluster together. In the spatial correlation pattern of local autocorrelation, H-H and L-L represent positive spatially correlated features, while H-L and L-H represent negative spatially correlated features.

3.2.2 ESTDA

Based on exploratory spatial data analysis (ESDA), the addition of a temporal dimension has led to the development of exploratory

spatio-temporal data analysis (ESTDA) (Rey & Janikas, 2009). The effectiveness of this method has been validated in revealing the spatio-temporal correlation patterns of urban land-use and ecological environment (ULGUE) in China (Ma et al., 2024). Currently, ESTDA is more widely applied in studies of land use and carbon emissions (Zhang et al., 2024; Xiang et al., 2025), with its main components including the LISA time path, LISA spatio-temporal transition, and spatio-temporal interaction visualization. In this paper, ESTDA is employed to investigate the spatial and temporal evolution of land surface temperature (LST).

Spatial weight matrix: In constructing the spatial weight matrix, the Rook adjacency method identifies neighboring spatial units based on shared boundaries (edge adjacency). This definition is straightforward. Compared with the Queen's method—which additionally includes diagonal adjacency—the Rook method considers only edge adjacency, thereby avoiding excessive connectivity. In this study, the Rook method is adopted to construct the spatial weight matrix.

LISA Time Path: Relative length (Γ_i), tortuosity (ε_i), and direction of motion (θ_i) are elements of the LISA time path, each of which can be calculated in the following ways.

$$\Gamma_{\mathrm{i}} = \frac{\mathrm{N}\sum_{t=1}^{T-1} d(L_{i,t}, L_{i,t+1})}{\sum_{i=1}^{N}\sum_{t=1}^{T-1} d(L_{i,t}, L_{i,t+1})} \tag{7}$$

$$\varepsilon_i = \frac{\sum_{t=1}^{T-1} d(L_{i,t}, L_{i,t+1})}{d(L_{i,1}, L_{i,T})} \tag{8}$$

$$\theta_i = \arctan\frac{\sum_j \sin\theta_j}{\sum_j \cos\theta_j} \tag{9}$$

Where N is the total number of cities, and T is the annual time interval. $L_{i,t}$ is the LISA coordinate of city i in year t. $\mathrm{d}(\mathrm{L_{i,t}}, \mathrm{L_{i,t+1}})$ is the distance city i moves from year t to t + 1, and $\mathrm{d}(\mathrm{L_{i,1}}, \mathrm{L_{i,T}})$ is the total distance it travels from the start to the end. If $\Gamma_{\mathrm{i}>1}$, city i moves relatively more than the average of all cities in terms of LISA-shifting distance. A larger Γ_{i} means more local spatial activity. When $\varepsilon_{\mathrm{i}}>1$, city i 's LISA movement is more curved than average. As ε_{i} rises, local spatial dependencies and structures become more dynamic and wavy. θ_i is the city's growth direction. From $0°$ to $90°$, the city and its neighbors grow together positively. From $90°$ to $180°$, the city grows slowly while neighbors grow fast. From $180°$ to $270°$, both decline. From $270°$ to $360°$, the city grows fast and neighbors grow slowly.

LISA spatio-temporal transition analysis: it investigates the evolution of local spatial association types for each spatial unit across different periods within the Moran scatter plot. This transition framework encompasses four types of transfer states, as summarized in Table 1.

Table 1
The primary categories of space–time transitions.

Type	Symbol	Symbolic Expressions
I	Self-stability,Neighbor-stability	$\mathrm{HH_t} \rightarrow \mathrm{HH_{t+1}}$,$\mathrm{HL_t} \rightarrow \mathrm{HL_{t+1}}$,$\mathrm{LL_t} \rightarrow \mathrm{LL_{t+1}}$,$\mathrm{LH_t} \rightarrow \mathrm{LH_{t+1}}$
II	Self-transition,Neighbor-stability	$\mathrm{HH_t} \rightarrow \mathrm{LH_{t+1}}$,$\mathrm{HL_t} \rightarrow \mathrm{LL_{t+1}}$,$\mathrm{LL_t} \rightarrow \mathrm{HL_{t+1}}$,$\mathrm{LH_t} \rightarrow \mathrm{HH_{t+1}}$
III	Self-stability,Neighbor-transition	$\mathrm{HH_t} \rightarrow \mathrm{HL_{t+1}}$,$\mathrm{HL_t} \rightarrow \mathrm{HH_{t+1}}$,$\mathrm{LL_t} \rightarrow \mathrm{LH_{t+1}}$,$\mathrm{LH_t} \rightarrow \mathrm{LL_{t+1}}$
IV	IVa:Self and neighborhood simultaneous transitions. IVb:Self and neighborhood reverse transitions	$\mathrm{HH_t} \rightarrow \mathrm{LL_{t+1}}$,$\mathrm{LL_t} \rightarrow \mathrm{HH_{t+1}}$. $\mathrm{HL_t} \rightarrow \mathrm{LH_{t+1}}$,$\mathrm{LH_t} \rightarrow \mathrm{HL_{t+1}}$

Rey(2010) further specified the measurement methods for spatial flux and spatial aggregation degree, aiming to quantify the degree of spatial aggregation. The specific formulas are as follows:

$$SF = \frac{Type_{\mathrm{II}} + Type_{\mathrm{III}}}{M} \tag{10}$$

$$SC = \frac{Type_{\mathrm{I}} + Type_{\mathrm{IV}a}}{M} \tag{11}$$

Among them, each parameter represents the quantity of each leap type in Table 1.

Spatio-temporal interaction visualization: it is employed to reveal the non-significant dynamic associations in ESTDA by mapping the known forms of spatio-temporal transitions in LST between cities, thereby better reflecting their spatio-temporal interaction patterns (Wang & Cheng, 2023). In this study, different colors are used for visualization, each corresponding to distinct dynamic association characteristics. Based on their values, these associations are categorized into four types:

1) Strong positive association (0.5 to 1.0)
2) Weak positive association (0 to 0.5)
3) Strong negative association (-1.0 to -0.5)
4) Weak negative association (-0.5 to 0)

A positive association indicates coordinated development between neighboring cities during the spatio-temporal transition process, while a negative association suggests a certain degree of spatio-temporal competition. A value of exactly 0 implies no dynamic association between adjacent cities.

3.2.3 Multifractal detrended cross-correlation analysis(MF-DCCA)

Multifractal Detrended Cross-Correlation Analysis (MF-DCCA), proposed by Zhou(2008), is a pioneering statistical methodology. This method is capable of detecting cross-correlations between two non-stationary sequences across disparate time scales.Firstly, define the two time series of land surface temperature (LST) and air pollutants as $\{x_i\}$ and $\{y_i\}$ respectively, where $\mathrm{i} = 1,2,\ldots,\mathrm{N}$. Secondly, the two series are divided into non-overlapping subsegments of equal length, where =N/s, and s represents the length of the time scale of the paper problem. Since N may not be divisible by s, it is necessary to repeat this method from the other end to avoid omission. For each sub-segment, the local trend is calculated using the least squares linear fit, and then averaging over all segments yields the qth-order fluctuation function $\mathrm{F_q(s)}$.It is important to note that q can assume any real value.

The generalized Hurst exponent, denoted $\mathrm{h(q)}$, is a measure of the correlation between time-series data. When $\mathrm{h(q)} = 0.5$, there is no correlation between the LST and air pollution sequences. However, when $\mathrm{h(q)} > 0.5$,there is a long-term power-law cross-correlation between the LST and air pollution sequences. Consequently, on specific temporal scales in the future, the occurrence of peaks in LST may result in peaks in air pollutants, thereby signifying a sustained long-term correlation between LST and air pollutants (Li et al., 2024).

In the event of $\mathrm{h(q)}$ decreasing monotonically as q increases, the cross-correlation between the two sequences will exhibit typical multifractal characteristics.The intensity of multifractality can be calculated from the range of $\mathrm{h(q)}$.The higher the intensity, the stronger

the multifractal characteristics, and the more pronounced the scale variability of the long-term persistence features of the cross-correlation between the two sequences will be under different levels of fluctuation.

In this study, seasonal components were extracted from both the STL decomposition and the pollutant time series using the STL method. Subsequently, MF-DCCA was applied to the deseasonalized series. The optimal bandwidth was determined through ten-fold cross-validation. Furthermore, a multi-scale analysis was performed by integrating the Continuous Wavelet Transform (CWT) with MF-DCCA.

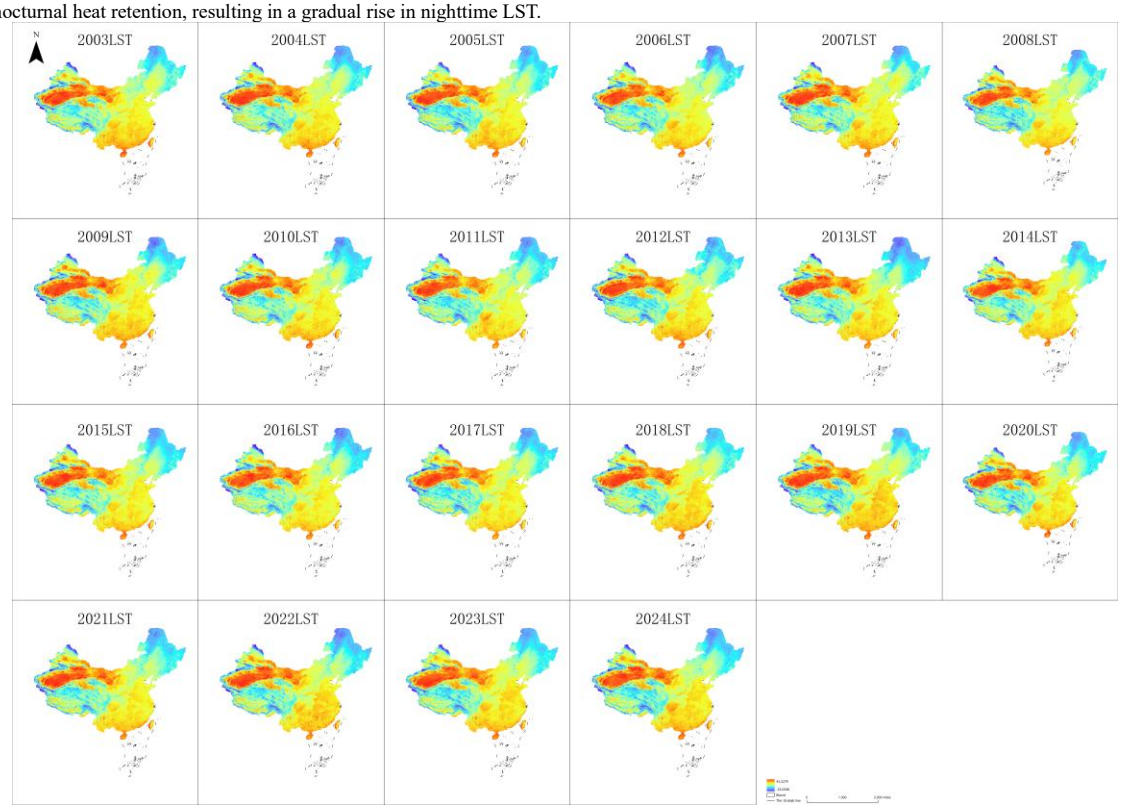
4. Results and discussion

4.1 LST time and spatial evolution results

As shown in Fig. 2, the spatial distribution of LST exhibits a clear day–night contrast between 2003 and 2024. During daytime, high LST values are concentrated in northwestern regions, whereas at night, the high-LST area shifts toward the southeast. This spatial variation can be linked to China's urban agglomeration development and its geographic setting.

In the northwest, inland location and dry air conditions allow for strong solar radiation penetration and rapid surface heating during the day. These factors, along with the distinctive surface characteristics of the Guanzhong Plain Urban Agglomeration—characterized by high radiation absorption and low albedo—contribute to elevated daytime LST. Urban construction materials such as asphalt and cement further enhance radiative absorption, intensifying the urban heat island effect. In contrast, the southeastern region benefits from oceanic temperature regulation at night. While the land cools rapidly, the ocean releases stored heat, which is then transported toward coastal areas via atmospheric circulation, moderating the nocturnal temperature drop. This maritime influence is evident in coastal cities like Shanghai (Yangtze River Delta) and Ningbo (Pearl River Delta), which maintain relatively stable and higher nighttime LST.

As illustrated in Fig. 3, daytime LST shows relatively stable variation over time, whereas nighttime LST displays a slight but discernible upward trend. These temporal patterns are associated with ongoing urban agglomeration development and global climate change. During the day, dynamic atmospheric circulation and frequent cold–warm air mass exchanges lead to fluctuating solar radiation reception. Urban expansion intensifies the heat island effect, further complicating daytime temperature stability—particularly evident in regions such as the Beijing-Tianjin-Hebei Urban Agglomeration, where extensive construction and industrial activity have altered surface properties and amplified thermal contrasts. At night, accelerated urbanization and rising greenhouse gas emissions enhance atmospheric insulation. In the Chengdu-Chongqing Economic Circle, for example, increased energy consumption and emissions contribute to greater nocturnal heat retention, resulting in a gradual rise in nighttime LST.



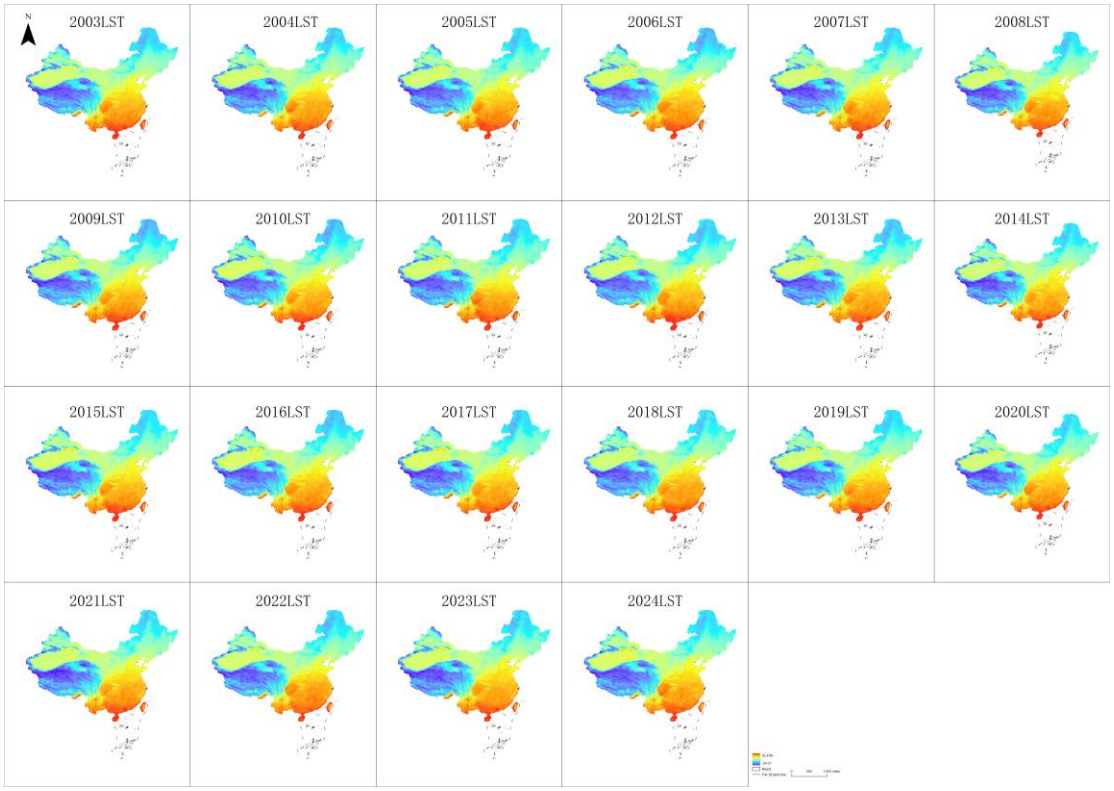


Fig.2. The overall distribution of LST in China from 2003 to 2024 (daytime on the top, nighttime on the bottom)

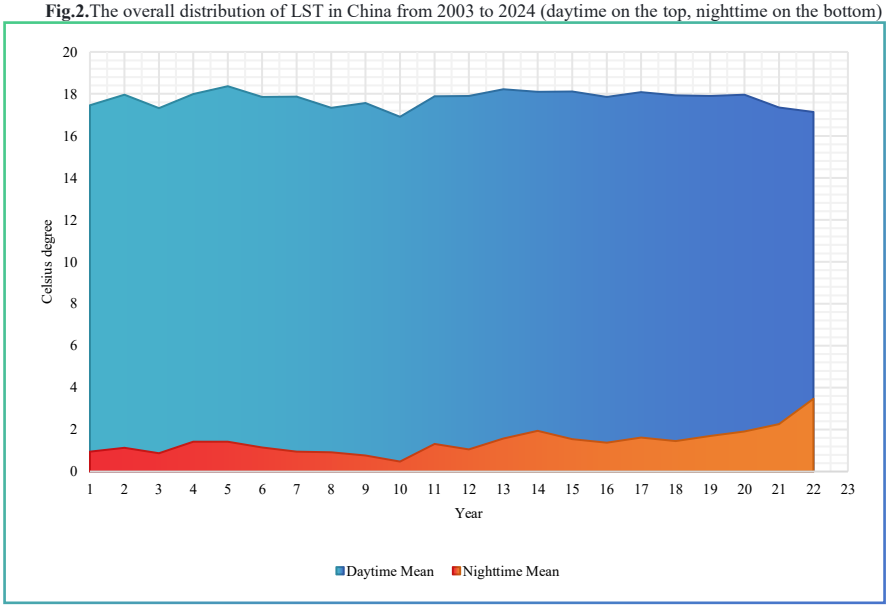


Fig.3. The Change Trend of LST in China from 2003 to 2024

4.2 Spatio-temporal variation of LST in China

As shown in Fig. 4(a), during the period 2003–2010, cities with a relative length greater than 1 were mainly distributed in northeast and southwest China. Notably, the relative length of the Harbin–Changchun Urban Agglomeration was particularly high. From 2010 to 2017, the number of cities with a relative length exceeding 1 increased significantly, especially in western China, where the Chengdu–Chongqing and Central Guizhou urban agglomerations exhibited notably high values. Between 2017 and 2024, even more cities surpassed the threshold of 1, with a marked rise in southeastern regions. The Chengdu–Chongqing Urban Agglomeration continued to show a prominent relative length, indicating significant and dynamic changes in the local spatial structure of LST in these areas over time.

From a socioeconomic perspective, during 2003–2010, traditional industries such as steel and machinery in the Harbin–Changchun Urban Agglomeration underwent transformation and technological upgrades. The renovation of large steel mills altered energy consumption and heat production patterns, thereby influencing urban LST. After 2010, with the deepening implementation of the Western Development Strategy, industrial relocation to the Chengdu–Chongqing and Central Guizhou urban agglomerations spurred the growth of electronics and equipment manufacturing. Industrial agglomeration increased urban heat output and altered its spatial distribution, leading to changes in LST patterns. From 2017 to 2024, sustained economic growth in southeastern China was accompanied by industrial diversification and upgrading, with rapid development in emerging sectors such as artificial intelligence and new energy. Continuous adjustments in urban functional zones and shifts in the distribution of industrial and population-related heat sources contributed to a more dynamic spatial structure of LST. Changes in regional energy structures and policies also played a role. For example, the northeast region shifted toward cleaner energy, reducing coal dependence and modifying heat emission patterns. Meanwhile, coordinated development

plans such as the Chengdu–Chongqing Economic Circle and the Harbin–Changchun urban agglomeration strategy promoted inter-city cooperation, integrated industrial networks, and improved transportation infrastructure, all of which influenced heat transfer and distribution among urban areas.

As illustrated in Fig. 4(b), changes in LST curvature are evident across three stages. The curvature values for most Chinese cities exceed 1, reflecting strong spatial dependence, distinct non-uniformity, and nonlinear characteristics in LST distribution, with a spatial pattern of "large dispersion and small aggregation." From 2003 to 2010, high-curvature cities were mainly located in the urban agglomerations of the Middle Reaches of the Yangtze River and the Guanzhong Plain. Accelerated urbanization in these regions led to large-scale expansion and surface alteration, where natural landscapes were replaced by built-up areas. This intensified the urban heat island effect and enlarged temperature differences between urban and surrounding areas, resulting in higher curvature values. Industrial growth and population concentration also increased energy consumption and waste heat release, further exacerbating LST variation.

From 2010 to 2017, high-curvature areas shifted to the Lanzhou–Xining Urban Agglomeration and Qinghai Province, and this pattern remained largely consistent through 2024. Meanwhile, curvature values rose significantly in the Yangtze River Delta and the Middle Reaches of the Yangtze River urban agglomerations. These changes can be attributed to accelerated energy exploration and infrastructure development in western regions—such as wind and photovoltaic power projects and transport network expansion—which altered the local surface energy balance and increased the complexity of LST distribution. In the Yangtze River Delta and the Middle Reaches of the Yangtze River, continued industrial modernization, growth in manufacturing, and rising energy consumption led to substantial release of industrial waste heat and combustion-related thermal discharge. This notably altered the regional thermal environment, especially in areas with concentrated high-energy-consuming industries, widening temperature contrasts and enhancing spatial variability in LST, thereby elevating curvature values.

As shown in Fig. 4(c), from 2003 to 2024, most cities exhibited synergistic development in LST. Synergistic positive growth was mainly concentrated in southeastern China, while synergistic negative growth dominated other regions. This indicates that LST across Chinese cities displays strong spatial integration, reflecting a general trend of coordinated development. However, the considerable number of cities showing synergistic negative growth also points to pronounced negative spatial integration. Given the interconnectedness of LST across regions, future policy efforts should emphasize cross-regional coordination—for example, through mechanisms linking upstream and downstream river basins or cities within the same urban agglomeration. Joint policy formulation and implementation in areas such as environmental protection and resource utilization should be promoted to foster regionally coordinated urban development.

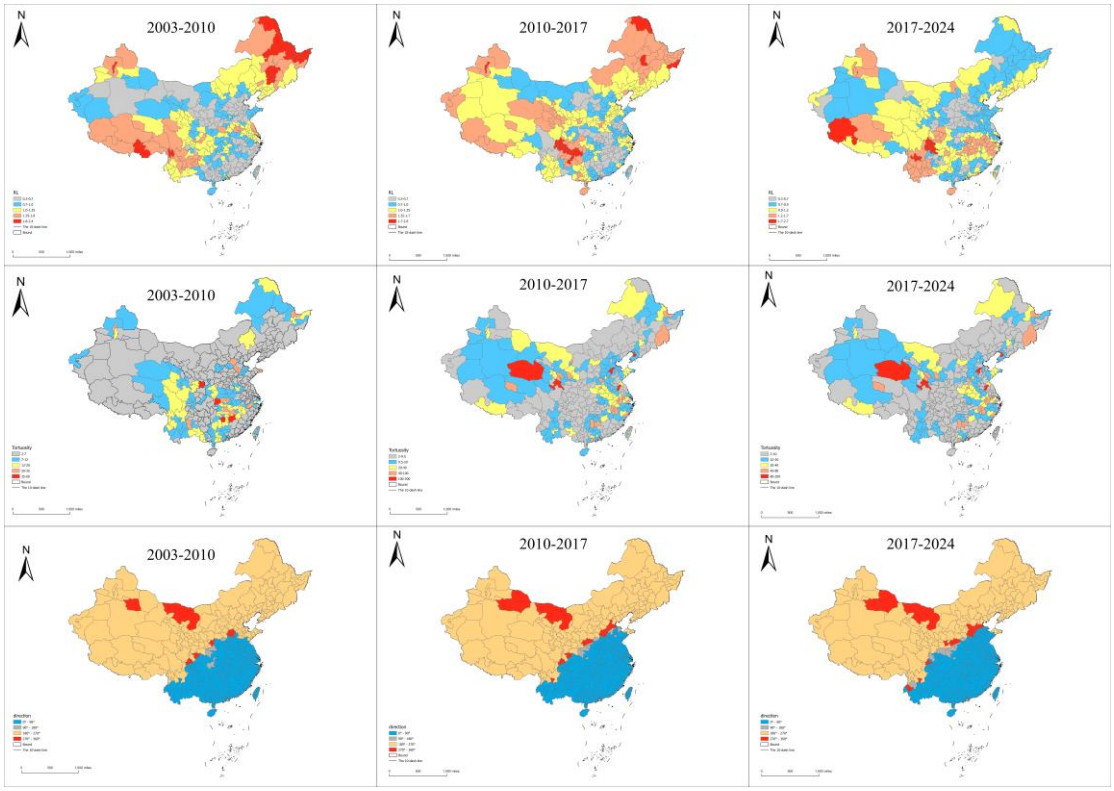


Fig.4. Geometric Characterization of the LISA Time Route(a) Relative Length
(b) Tortuosity(c) Movement Direction

Spatio-temporal leap analysis is further used to examine the evolution of local spatial association types of LST. As shown in Table 2, the predominant transition type across all three periods is Type 1, with probabilities of 96%, 95%, and 97%, respectively. This indicates that neither individual cities nor their neighboring units underwent significant changes in local spatial association. The result implies a relatively stable overall spatial structure of LST throughout the study period and highlights notable path dependence.

According to existing literature (Ma et al., 2024), spatial cohesion (SC) exceeding 70% suggests a strongly cohesive spatial distribution. As presented in Table 2, the SC values for the three stages all surpass 95%, and Type 1 transitions remain highly frequent in each period. This confirms that most cities have not experienced substantial spatio-temporal shifts. Therefore, the spatial layout of LST demonstrates a high degree of cohesion, and the current spatial distribution pattern is unlikely to change significantly in the short term.

Table 2

Spatio-temporal leaps and probability matrices for different stages of LST

Period of time	t/t+1	HH	LH	LL	HL	Type	Quantity	Percentage	SF	SC
2003-2010	HH	0.545	0.003	0	0.003	Type1	359	0.96	0.019	0.98
	LH	0.005	0.008	0	0	Type2	3	0.008		
	LL	0.008	0.003	0.39	0.003	Type3	4	0.011		
	HL	0.016	0	0	0.016	Type4	8	0.021		

2010-2017	HH	0.567	0.003	0	0.005	Type1	356	0.95	0.035	0.96
	LH	0.003	0.011	0	0	Type2	7	0.019		
	LL	0.019	0.008	0.353	0.011	Type3	6	0.016		
	HL	0	0	0	0.021	Type4	5	0.013		
2017-2024	HH	0.58	0.003	0	0.003	Type1	362	0.97	0.019	0.98
	LH	0.008	0.013	0	0	Type2	0	0		
	LL	0	0.005	0.342	0.005	Type3	7	0.019		
	HL	0.005	0	0.003	0.029	Type4	5	0.013		

The results of spatio-temporal interaction visualization are presented in Fig. 5. The dynamic correlation characteristics of LST in most cities show a moderately positive correlation, while a small number of cities exhibit a strongly positive correlation. These positively correlated cities are mainly distributed in eastern China, extending from the Liaozhongnan Urban Agglomeration in the north to the Middle Reaches of the Yangtze River Urban Agglomeration in the south. This finding indicates that during the spatio-temporal transition of LST, most cities—especially those in eastern China—demonstrate coordinated development with a high degree of spatio-temporal correlation.

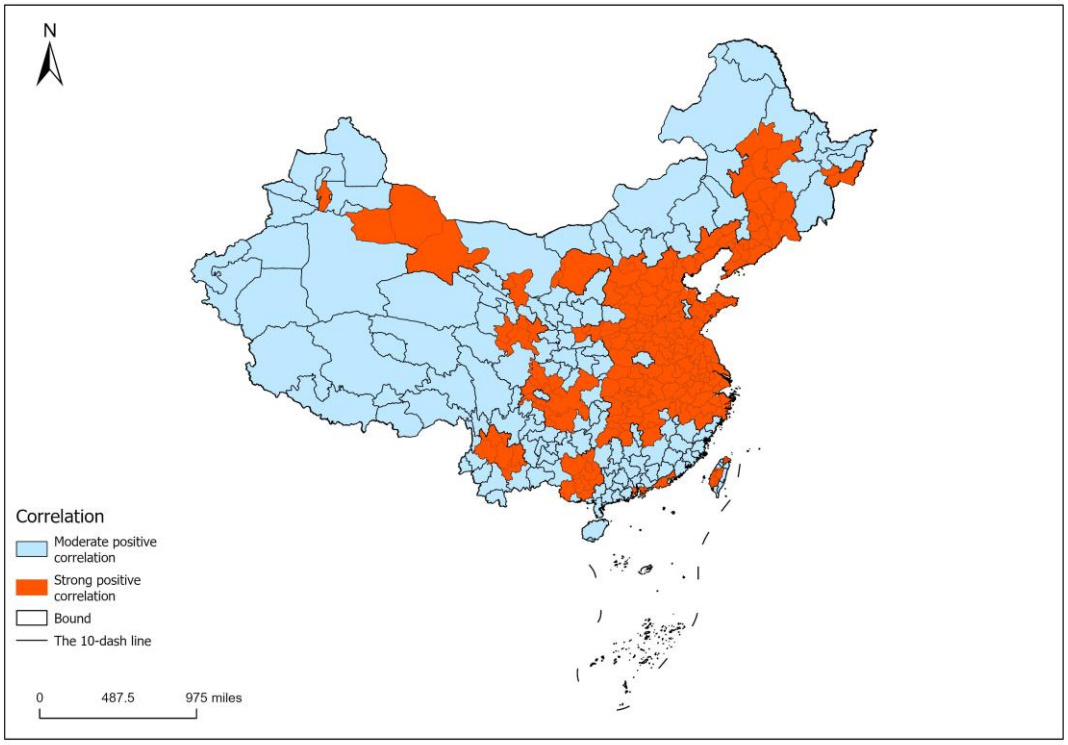


Fig.5. Spatio-temporal interaction visualization

4.3 Spatio-temporal variation of air pollutants in China

4.3.1 Spatial variation of air pollutants in China

The global Moran's I was utilized to assess the spatial autocorrelation of three air pollutants from 2003 to 2024, as depicted in Table 3. The results indicate a substantial spatial correlation within the 99.9% confidence interval for the air pollutants. Notably, the Moran's I values for $PM_{2.5}$,O_3 and PM_{10} demonstrate a generalized trend of initial increase followed by subsequent decrease, while the Moran's I value for generally increases. This finding suggests that the implementation of various air pollution prevention and control measures has led to a certain degree of dispersion of emission sources for $PM_{2.5}$,O_3 and PM_{10}. However, it is important to note that the ongoing increase in industrial production, transportation, and other activities has resulted in a continuous rise in emissions of precursors such as nitrogen oxides and volatile organic compounds. Under favourable conditions, such as the presence of sunlight, these precursors are more likely to react and generate pollutants which can then be accumulated in specific areas.

Table 3

Moran's I of air pollutants, 2003-2024

Year	PM2.5	PM10	Ozone
2003	0.871	0.866	0.827
2004	0.861	0.857	0.833
2005	0.869	0.872	0.832
2006	0.874	0.867	0.804
2007	0.87	0.86	0.802
2008	0.872	0.87	0.811
2009	0.874	0.87	0.82
2010	0.861	0.866	0.823
2011	0.875	0.868	0.783
2012	0.889	0.882	0.835
2013	0.872	0.869	0.777
2014	0.877	0.871	0.811
2015	0.879	0.876	0.8
2016	0.873	0.862	0.865

2017	0.872	0.858	0.922
2018	0.871	0.861	0.915
2019	0.867	0.832	0.915
2020	0.834	0.804	0.92
2021	0.827	0.839	0.9
2022	0.835	0.859	0.923
2023	0.838	0.836	0.91
2024	0.838	0.838	0.892

This study selected the two endpoints of the observation period, 2003 and 2024, as key time points for comparison. The results of cold spot and hot spot analysis (Fig. 6) indicate the following:

From 2003 to 2024, the spatial extent of cold spots slightly exceeded that of hot spots. Hot spots were widely distributed across the Beijing–Tianjin–Hebei, Taiyuan, and Central Plains urban agglomerations, whereas cold spots were mainly concentrated in Tibet and Yunnan. During this period, hot spot areas expanded in western Xinjiang, while cold spot areas also showed expansion in Tibet and Yunnan. Both cold and hot spots exhibited an overall westward expansion trend.

By 2024, the spatial coverage of hot spots surpassed that of cold spots. Hot spots were primarily distributed across cities in northern China, including the Wulumuqi–Changji–Sheihezi, Ningxia Yellow River–Riverside, and Lanzhou–Xining urban agglomerations. In contrast, cold spot areas extended from Yunnan to eastern Tibet, showing an outward spreading pattern.

Between 2003 and 2024, the relative spatial extent of hot spots gradually increased relative to cold spots, accompanied by notable shifts in their geographic distribution. Earlier hot spot regions such as the Hohhot–Baotou–Ordos–Yulin and Ningxia Yellow River–Riverside urban agglomerations were succeeded by areas associated with the Central Plains and Taiyuan urban agglomerations (note that Tibet is not classified as an urban agglomeration in this analysis). Similarly, cold spot distribution also shifted: areas previously identified in parts of the Chengdu–Chongqing and Central Guizhou urban agglomerations were replaced by regions related to the West Coast of Taiwan Strait and Pearl River Delta urban agglomerations (again, Tibet is not considered an urban agglomeration in this context).

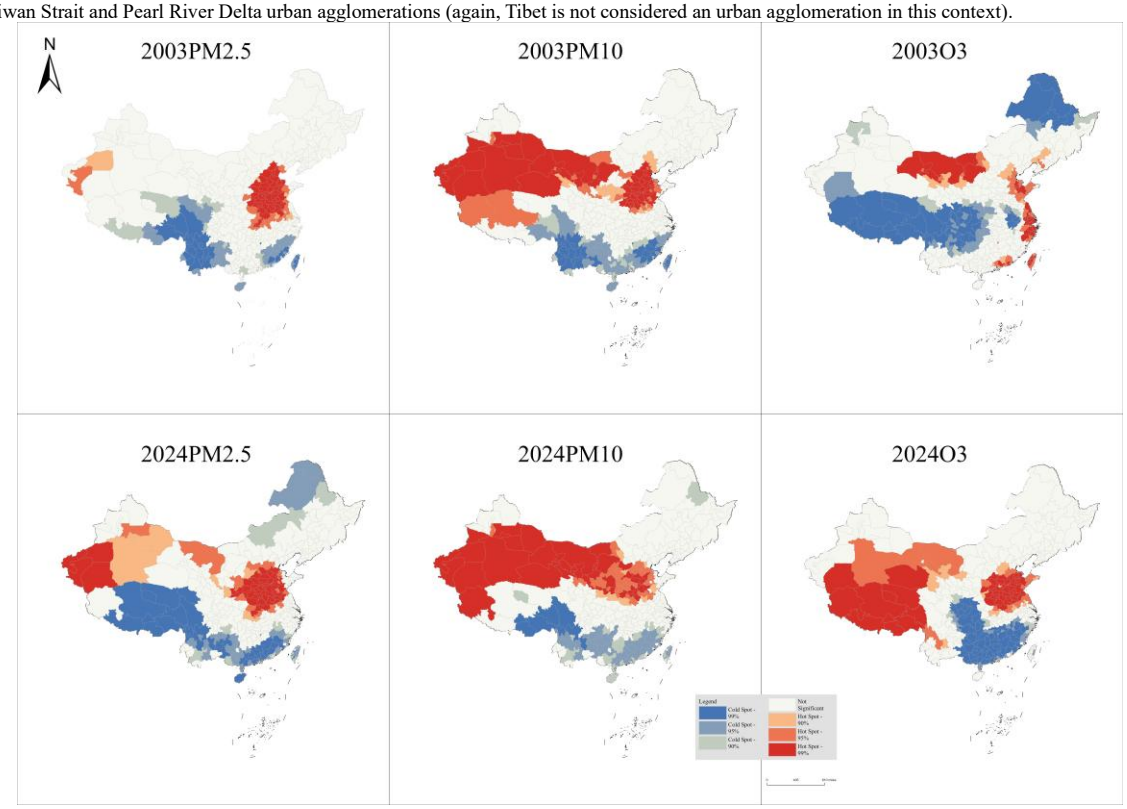


Fig.6. Analysis of cold and hot spots of pollutant concentration

The spatial agglomeration of urban pollutant concentrations is visualized using kernel density mapping (Fig. 7). The results indicate that all three pollutants were primarily concentrated in the Central Plains urban agglomeration, the Yangtze River Delta urban agglomeration, and Taiwan Province. From 2003 to 2024, the emission distribution of these pollutants exhibited a pattern of initial expansion followed by contraction. This trend reflects China's environmental policy evolution: following a period of rapid industrialization and urbanization that led to significant pollution and climate-related challenges, the country has actively pursued green development and environmental governance, implemented strict regulations on pollutant emissions, and achieved notable progress in emission control.

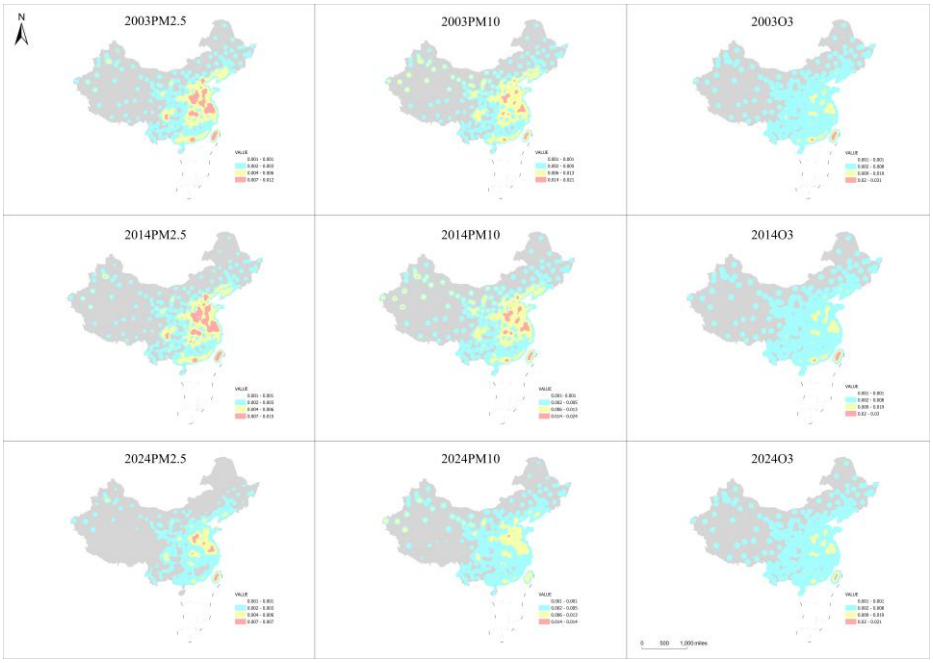
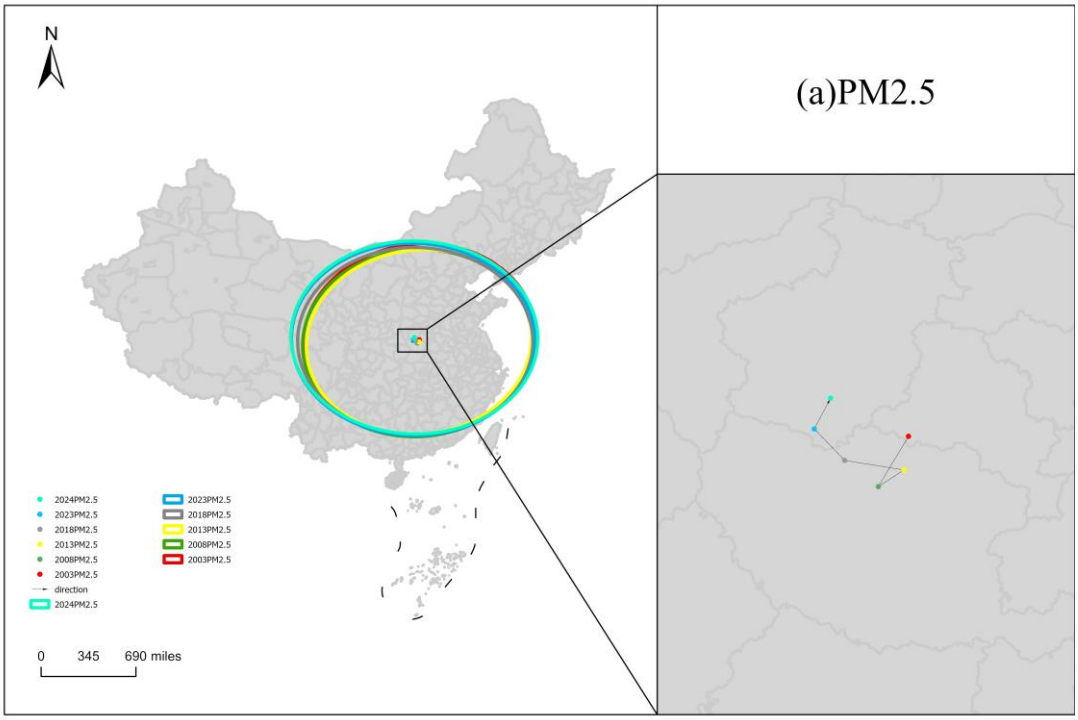
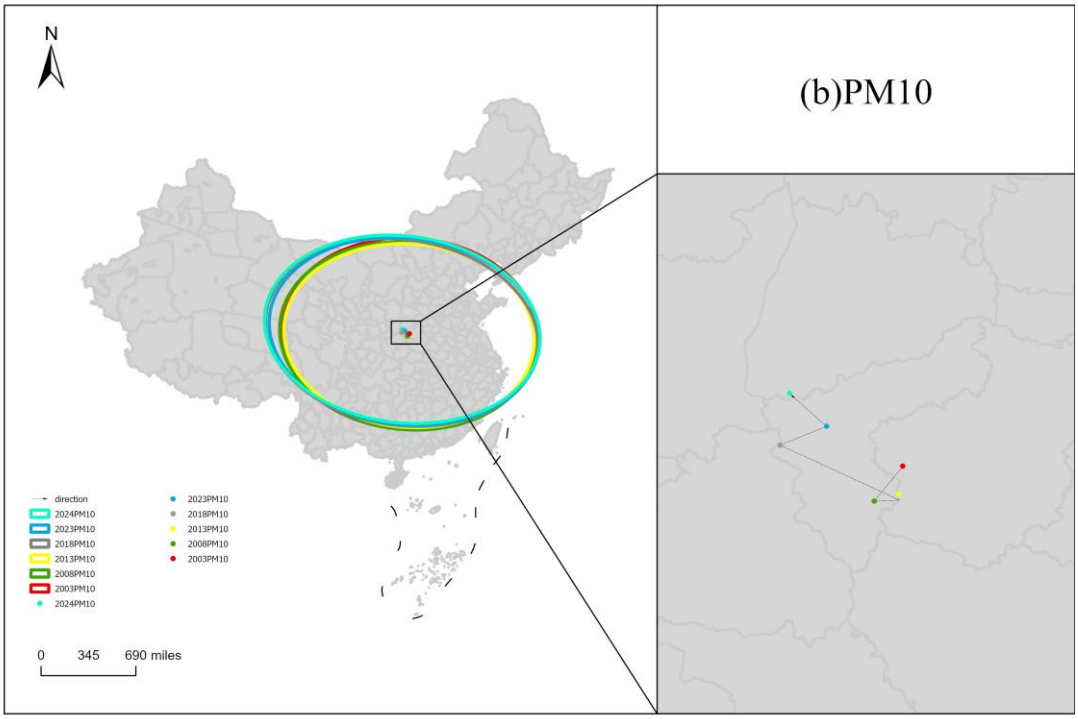


Fig.7. The evolution of cold and hot spots in Chinese cities in 2003 and 2024

The results of the Standard Deviation Ellipse (SDE) analysis (Fig. 8) show that pollutant concentrations in China generally exhibited an east–west-oriented spatial distribution during the study period. In 2003, the centroids of $PM_{2.5}$ and PM_{10} concentrations were located in Pingdingshan City and Luoyang City, Henan Province, respectively, while that of O_3 was situated in Luoyang City, Henan Province. By 2024, these centroids had shifted to Luoyang City (Henan Province) and Yuncheng City (Shanxi Province), respectively. It is noteworthy that the concentration centroid of another pollutant (e.g., specify pollutant if applicable) remained in Nanyang City, Henan Province throughout the observation period.

To better illustrate the migration trajectory of the centroids, intermediate nodes between 2003 and 2024 were included in the analysis. This spatial shift can be attributed to the relocation of traditional high-pollution and high-energy-consumption industries from eastern to central and western regions, driven by industrial upgrading and increasingly stringent environmental regulations in eastern China. Additionally, the abundant coal resources in the northwest have spurred the development of energy extraction and processing industries, further influencing the westward movement of pollutant concentration centroids.





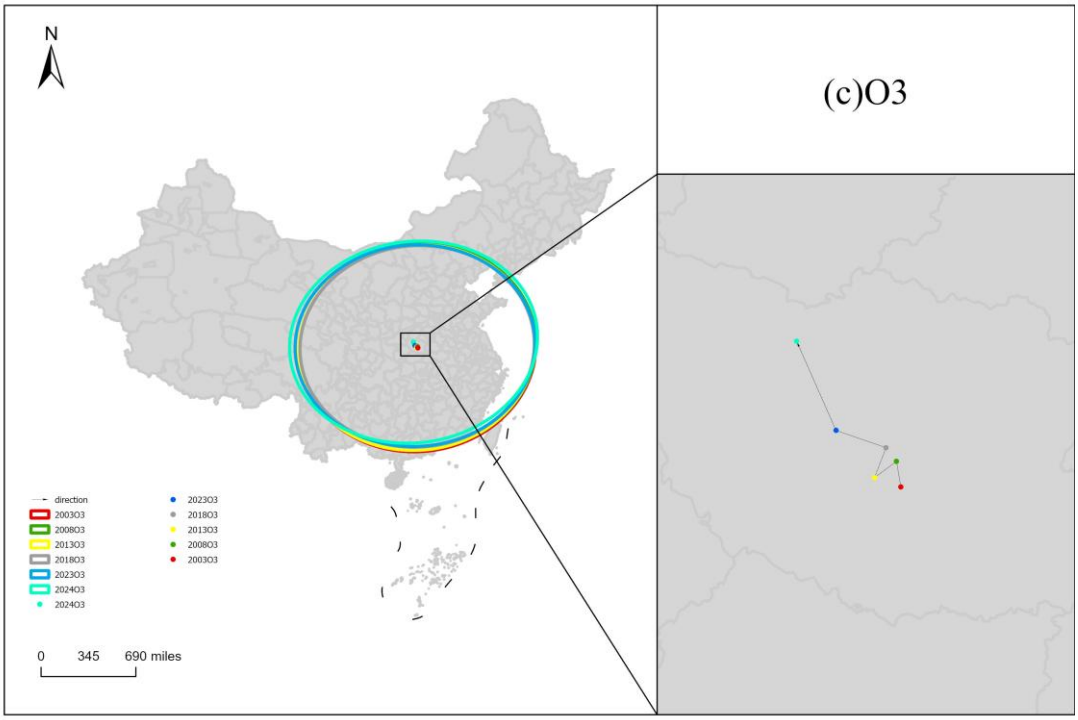


Fig.8. The distribution of Chinese cities and the standard deviation ellipse

The Pearson correlation coefficients among three pollutants across China's four major economic regions from 2003 to 2024 are shown in Fig. 9. The coefficient between the western and northern regions is the smallest, while that between the central and eastern regions is the largest. This indicates that pollutant concentrations in the western and northern regions exhibit the weakest interregional correlation, whereas the central and eastern regions show the strongest correlation.

This pattern can be attributed to more intensive environmental governance and relatively well-developed interregional cooperative mechanisms in the central and eastern regions. For example, cross-regional environmental protection collaborations have been established in areas such as the Yangtze River Delta and the Pearl River Delta. As a result, pollutant concentrations in these regions are influenced by similar policy frameworks, enhancing their correlation.

Although the western region has also made continuous efforts in environmental protection, its vast territory leads to variations in environmental management levels and policy implementation intensity across different areas. Furthermore, environmental policies in the west are less synchronized with those of other regions, resulting in weaker correlation with pollutant changes elsewhere. The northern

region implements environmental policies with distinct regional characteristics, such as specific measures targeting winter heating pollution. Differences in policy priorities and implementation effectiveness between the northern and western regions further contribute to the low correlation in pollutant concentrations between the two.



Fig.9. Pearson coefficients among the four regions($PM_{2.5}$,PM_{10},O_3)

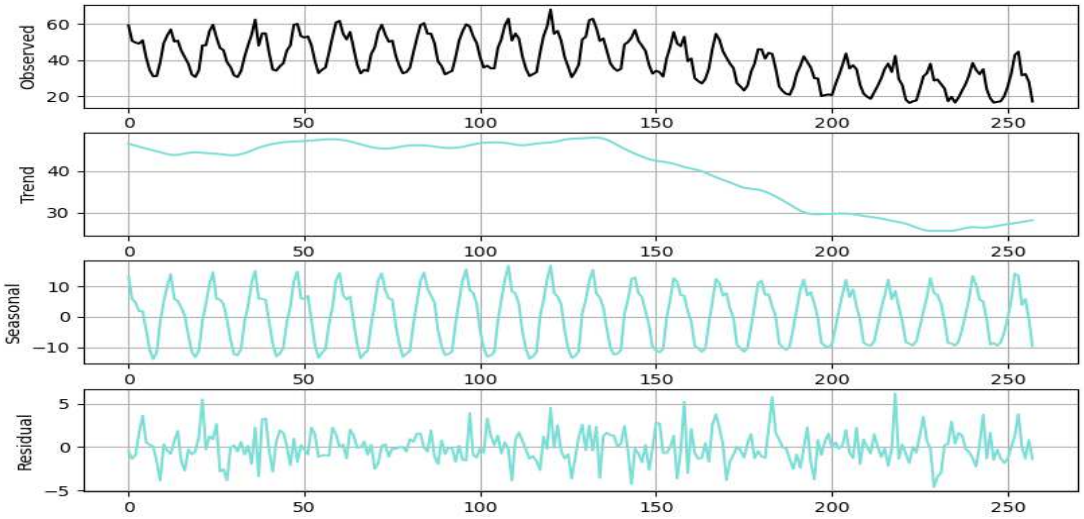
4.3.2 Temporal variation of air pollutants in China

As shown in Fig. 10, the original time series and STL-decomposed components of three air pollutants from 2003 to 2024 are clearly displayed. The original pollutant series exhibit distinct seasonal patterns, which are intertwined with long-term trends, making it difficult to directly analyze their underlying trend components. The STL method effectively separates the long-term trend from the seasonal and residual components for each pollutant.

The long-term trends of $PM_{2.5}$, O_3, and PM_{10} show an overall increase from 2003 to 2015, followed by a decline from 2015 to 2024. The trend of O_3 remained relatively stable from 2003 to 2017, rose between 2017 and 2022, and then decreased notably from 2022 to 2024.

Seasonal fluctuations in $PM_{2.5}$, O_3, and PM_{10} are clearly visible, following a consistent 12-month cycle. The residual terms of all three pollutants display random variations, yet their amplitude correlates closely with the original series.

These findings imply that, as coordinated air pollution control measures have intensified, reductions in ozone precursors such as NO_x and VOCs have limited the availability of reactants for ozone formation, contributing to the observed decline in ozone concentrations after 2022.



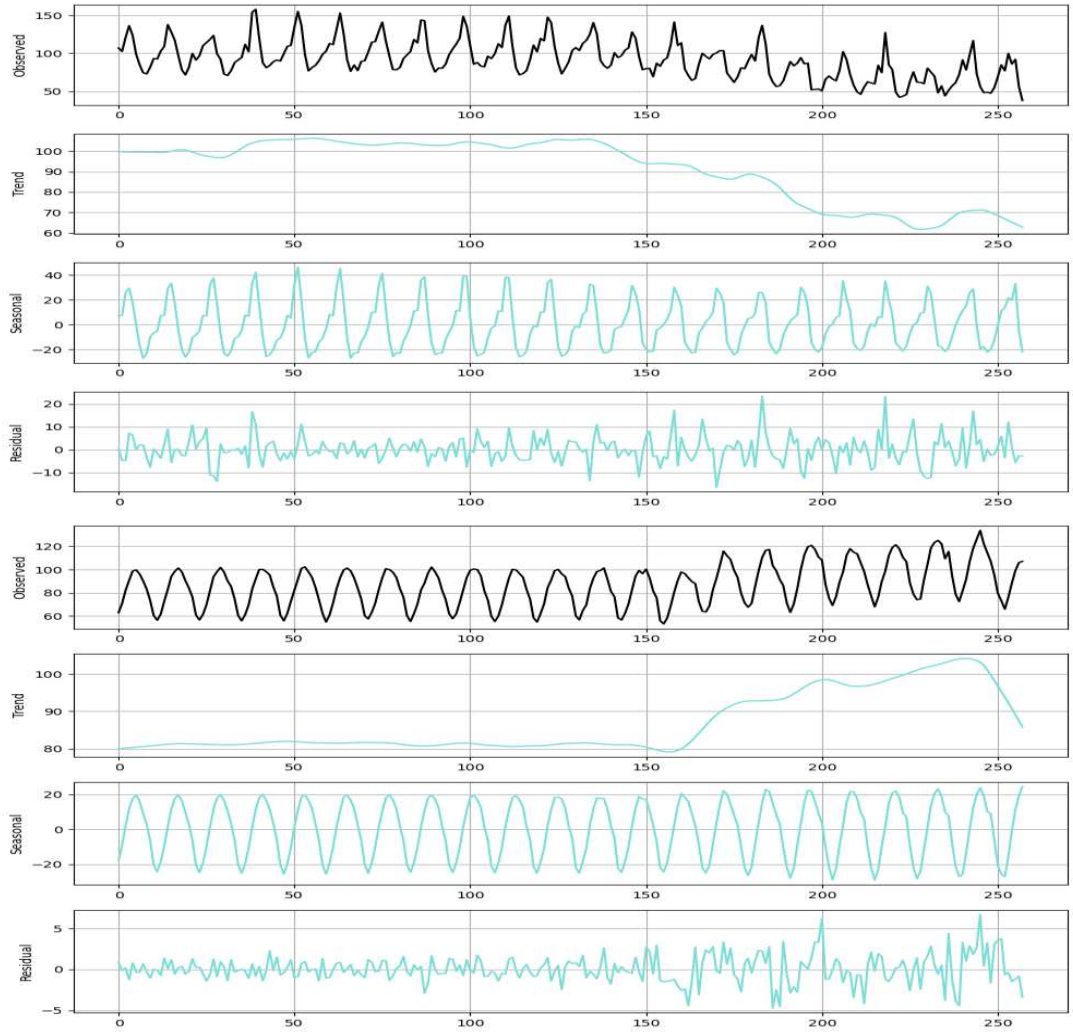


Fig.10.STL decomposition results of $PM_{2.5}$, PM_{10} and O_3 from 2003 to 2024

4.4 Relationship between LST and air pollutants in China

The Multifractal Detrended Cross-Correlation Analysis (MF-DCCA) method was employed to investigate the correlations among the variables. As illustrated in Fig. 11, a linear relationship exists between $PM_{2.5}$, PM_{10}, O_3, and LST, indicating scale-invariant fluctuations across these parameters. In other words, their variation patterns remain similar over different time scales. This linear scaling behavior provides a foundation for multifractal analysis, suggesting the presence of cross-correlations or power-law dependencies in the data.

The correlation strength between pollutants and LST generally decreases with increasing time scales. Values for $q < 0$ are consistently larger than those for $q > 0$, indicating that small fluctuations exhibit more persistent cross-correlation than large fluctuations. Moreover, cross-correlation diminishes as the scaling order q increases for both small and large fluctuations, implying weaker correlation for larger variations.

The Hurst exponent h(2) falls between 0.5 and 1, reflecting persistent cross-correlation in the time series, meaning that past trends are likely to continue in the future. The non-linear pattern of the scaling function further reveals multifractal characteristics in the fluctuations between $PM_{2.5}$, PM_{10}, O_3, and LST. Multifractality suggests that the statistical properties of fluctuations vary across different scales rather than conforming to a single fractal structure.

The multifractal spectrum displays a left-skewed inverted parabolic shape, indicating that larger fluctuations dominate the fractal properties of the series. That is, higher-amplitude variations contribute more substantially to the overall multifractal behavior. This left skewness is corroborated by $r < 1$ in Table 5. The multifractal intensity, denoted by Δh in the last row of Table 4, is significantly greater than zero, confirming a strong multifractal pattern in the cross-correlations between LST and each pollutant. However, notable differences exist among the pollutant–LST pairs: O_3–LST exhibits the highest multifractality, followed by PM_{10}–LST, while $PM_{2.5}$–LST shows the lowest intensity. These results are further supported by the width of the multifractal spectrum in Table 5, where O_3 presents the highest variability in both small and large fluctuations, reflecting a more heterogeneous and irregular distribution. PM_{10} ranks second, and $PM_{2.5}$ the weakest.

The non-zero width of the multifractal spectrum confirms a clear deviation from a random walk process. Additionally, the relatively high values (ranging from 1.3854 to 1.7582) in Table 5 indicate that correlations between pollutants and LST are influenced by prior system states and demonstrate considerable regularity over time.

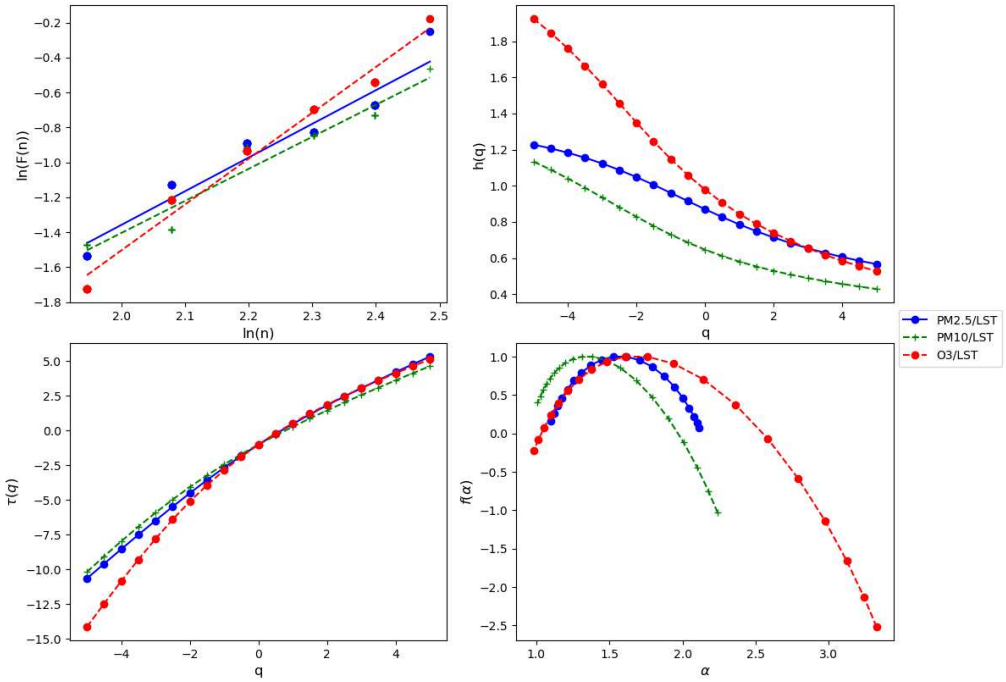


Fig.11. Analysis results of MF-DCCA

Table 4
Hurst Exponent ranging from q= -5 to q=5

q = -5	1.2273	1.1335	1.9239
q = -4	1.1826	1.0397	1.7589
q = -3	1.1230	0.9350	1.5620
q = -2	1.0476	0.8280	1.3493
q = -1	0.9602	0.7293	1.1476
q = 0	0.8698	0.6460	0.9780
q = 1	0.7857	0.5800	0.8438
q = 2	0.7133	0.5288	0.7383
q = 3	0.6537	0.4887	0.6535
q = 4	0.6053	0.4561	0.5842
q = 5	0.5661	0.4286	0.5269
Δh	**0.6612**	**0.7049**	**1.3970**

Table 5
Statistics from the MF-DCCA

Parameter pair	α0	α	r
PM2.5-LST	1.6148	1.0149	0.9352
PM10-LST	1.3854	1.2309	0.4407
Ozone-LST	1.7582	2.3464	0.4950

The long-range cross-correlation between pollutants and land surface temperature (LST) indicates that each time series retains a long-term memory of its own past values as well as those of the other series. Moreover, an increase (or decrease) in pollutant concentration is likely to coincide with a corresponding increase (or decrease) in LST. The h(2) values for each pollutant–LST pair all exceed 0.5, reflecting strong multifractal cross-correlations.

As shown in Fig. 12, wavelet analysis results reveal distinct time–frequency characteristics for different pollutants and LST. For $PM_{2.5}$, wavelet coefficients show enhanced strength around 2015 at scales of approximately 5–10, indicating more pronounced concentration fluctuations during this period. Around 2024, similar significant variations are observed within scales of 5–15, suggesting strong signal responses in this scale interval. PM_{10} exhibits notably elevated wavelet coefficients around 2008, 2013, and 2019 at scales near 5–10, pointing to substantial concentration fluctuations at these frequencies. For O_3, after 2015—particularly near 2024—coefficients intensify and vary considerably at scales of about 5–10, revealing a discernible trend in ozone concentration. LST wavelet coefficients display consistent and significant intensity across scales of 5–15, reflecting both the stability of surface temperature and its notable fluctuations within this range. These findings imply that different environmental variables ($PM_{2.5}$, PM_{10}, O_3, and LST) exhibit unique variation patterns at specific times and scales, which may be closely related to climatic conditions, human activity intensity, and industrial emissions in different years.

As illustrated in Fig. 13, the h(q) curves at smaller scales reflect short-term local characteristics of the time series. In the atmospheric environment, pollutant emission sources are relatively stable over short periods, and meteorological conditions vary little, leading to strong correlation and continuity between pollutant concentrations and LST, hence higher h(q) values. In contrast, h(q) curves at larger scales correspond to long-term overall characteristics. Over extended periods, meteorological conditions may change periodically (e.g., seasonally), and pollutant emission sources may shift (e.g., due to seasonal heating variations), complicating the relationship between pollutant concentrations and LST and weakening their correlation and continuity, thus resulting in lower h(q) values. The multiscale h(q) variations for the three pollutants are greater when $q < 0$ and smaller when $q > 0$. Most h(q) curves exceed 0.5 at $q = 2$ and exhibit mutual oscillation across scales. This supports the earlier conclusion that pollutants are more strongly correlated with LST in the short term and further highlights the robust, dynamic nature of multiscale interactions between LST and air pollutants.

As shown in Fig. 14 and Table 6, curves at different scales are distributed dispersedly without obvious overlap, indicating that the multifractal properties between pollutants and LST differ significantly across scales. The complexity of their multiscale relationship diminishes as scale increases, consistent with previous findings. Compared to other pollutants, O_3 and LST exhibit the most complex multiscale relationship. At smaller scales, $PM_{2.5}$ and LST show a more complex relationship than PM_{10} and LST, whereas at larger scales, the relationship becomes simpler than that of PM_{10} and LST. This suggests that the interaction between pollutants and LST is scale-dependent, varying considerably across scales, which must be fully considered to accurately characterize their interdependencies.

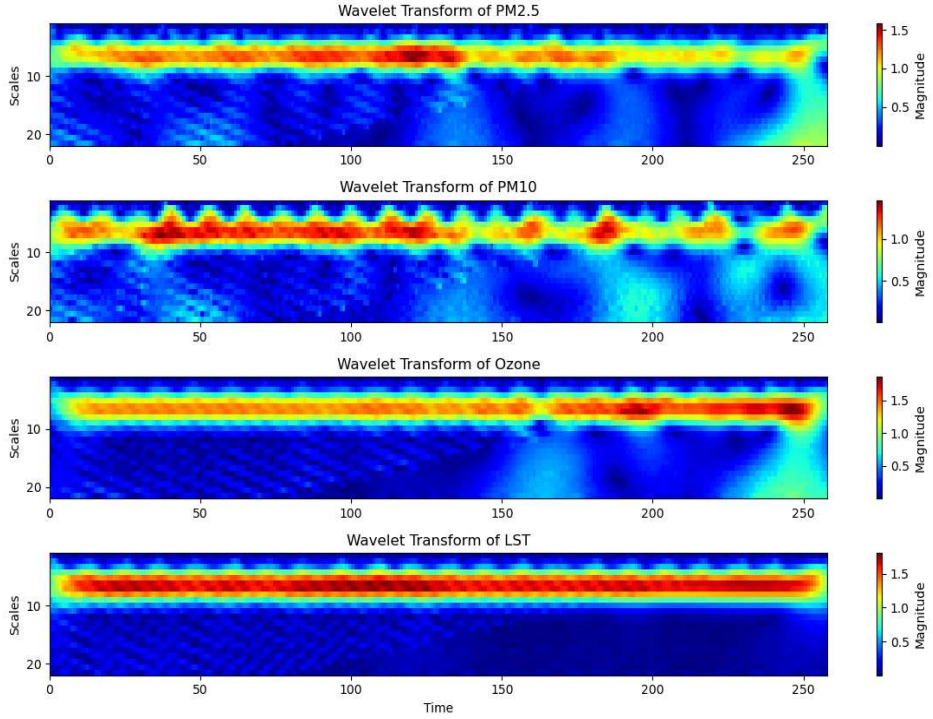


Fig.12. Analysis results of CWT

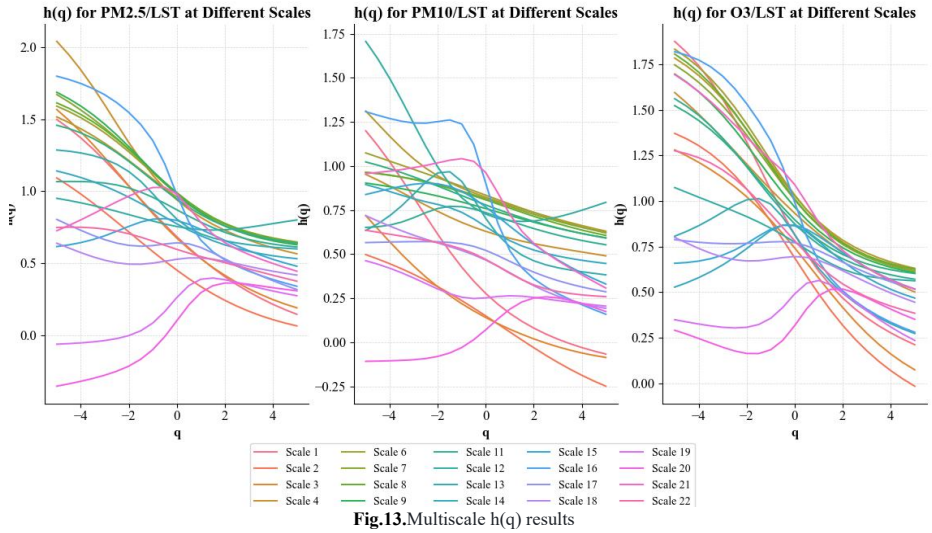


Fig.13. Multiscale h(q) results

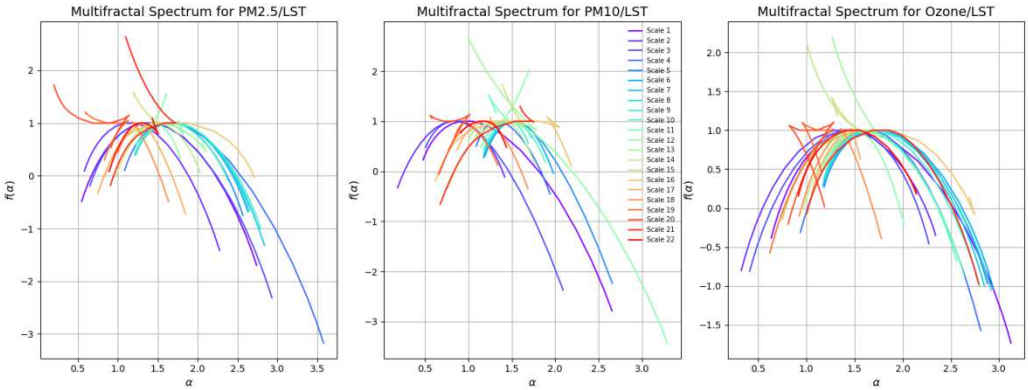


Fig.14. Multiscale f(α) results

Table 6
Multiscale multicollinearity complexity analysis

Scale	PM2.5	PM10	Ozone
1	2.19	2.18	2.49
2	1.69	1.24	2.02
3	2.27	1.58	1.86
4	2.49	0.85	1.87
5	1.34	1.47	1.69
6	1.41	0.81	1.77
7	1.61	0.53	1.66
8	1.42	0.55	1.72
9	1.57	0.5	1.62
10	1.15	0.71	1.34
11	0.60	0.33	1.46
12	0.36	1.92	0.80
13	0.85	0.78	1.03
14	0.88	0.69	0.6
15	0.53	0.88	0.57
16	1.87	1.57	1.99
17	1.10	0.41	0.51
18	0.63	0.91	0.85
19	0.54	0.5	0.66
20	0.94	0.46	0.48
21	0.82	1.08	1.79
22	0.53	0.61	1.23

5.Conclusions

In this study, the spatiotemporal evolution of LST and its correlation with $PM_{2.5}$, PM_{10}, and O_3 across China from 2003 to 2024 were comprehensively examined using monthly data. By innovatively integrating ESTDA and STL to investigate spatiotemporal patterns, and applying MF-DCCA to quantify their relationships, several key conclusions can be drawn.

First, seasonal variations in pollutant concentrations exhibited distinct characteristics. O_3 concentrations peaked during summer months, whereas PM_{10} and $PM_{2.5}$ levels were higher in winter. Spatially, the weakest correlations in pollutant concentrations were observed between western and northern regions, while central and eastern China showed strong interregional correlations. Additionally, the UHI effect was particularly pronounced in the Yangtze River Delta and Middle Reaches of the Yangtze River urban agglomerations.

Second, fluctuations and interactions among the three pollutants and LST displayed multifractal features and persistent cross-correlations, indicating highly complex interdependencies. Among these relationships, the coupling between O_3 and LST exhibited the strongest multifractality and scale-dependent correlation.

Third, evidence of multifractality suggests that LST can serve as a useful predictor for future pollutant concentrations, with better performance in short-term forecasting.

The findings of this study offer valuable implications for both scientific research and policy formulation. Understanding the spatiotemporal dynamics of LST and key pollutants can enhance comprehension of China's urban heat island effect over the past two decades and support evaluation of related environmental policies. Furthermore, revealing the complex interactions between LST and air pollutants can inform the inclusion of additional covariates in air quality prediction models, thereby improving their accuracy and reliability.

6.Limitations and future paper

While this study offers valuable insights into the spatiotemporal evolution of LST and its correlation with $PM_{2.5}$, PM_{10}, and O_3 in China, several limitations should be acknowledged.

Although a combination of analytical methods—including STL, ESTDA, and MF-DCCA—was applied, inherent methodological constraints may have influenced the results. The assumptions underlying these techniques may not fully reflect complex real-world conditions, which could introduce some bias. Future research could integrate more advanced modeling approaches, such as deep neural networks or random forests, to improve the robustness and accuracy of the findings.

Moreover, this analysis did not account for other influential variables, such as meteorological factors (e.g., humidity, wind speed) and anthropogenic activities (e.g., transportation, industrial emissions). Their exclusion may oversimplify the studied relationships. It is therefore recommended that subsequent work incorporate these elements to more comprehensively examine the links between LST and air pollutants. Additional factors such as land cover characteristics and urban forest structure should also be considered to further clarify these interactions.

By integrating a broader range of driving factors, future studies can better support long-term urban greening strategies, enhance the understanding of air quality dynamics and environmental impacts, and ultimately inform more effective policy-making and environmental management. Such efforts will contribute to the development of targeted urban planning and environmental protection policies, promoting sustainable urban development.

Declaration of Competing Interest

The authors declare that they have no known competing financial interests or personal relationships that could have appeared to influence the work reported in this paper.

Data availability

Data will be made available on request.

References

Liu, H., Huang, B., Gao, S., Wang, J., Yang, C., & Li, R. (2021). Impacts of the evolving urban development on intra-urban surface thermal environment: Evidence from 323 Chinese cities. *Science of the Total Environment, 771,* 144810. https://doi.org/10.1016/j.scitotenv.2020.144810

Chen, W., Zeng, J., & Li, N. (2021). Change in land-use structure due to urbanisation in China. *Journal of Cleaner Production, 321,* 128986. https://doi.org/10.1016/j.jclepro.2021.128986

Qi, G., Che, J., & Wang, Z. (2023). Differential effects of urbanization on air pollution: Evidences from six air pollutants in mainland China. *Ecological Indicators, 146,* 109924. https://doi.org/10.1016/j.ecolind.2023.109924

Tesfamariam, S., Govindu, V., & Uncha, A. (2023). Spatio-temporal analysis of urban heat island (UHI) and its effect on urban ecology: The case of Mekelle city, northern Ethiopia. *Heliyon,* e13098. https://doi.org/10.1016/j.heliyon.2023.e13098

Sabrin, S., Karimi, M., Fahad, M. G. R., & Nazari, R. (2020). Quantifying environmental and social vulnerability: Role of urban Heat Island and air quality, a case study of Camden, NJ. *Urban Climate, 34,* 100699. https://doi.org/10.1016/j.uclim.2020.100699

Elhabodi, T. S., Yang, S., Parker, J., Khattak, S., He, B.-J., & Attia, S. (2023). A review on BIPV-induced temperature effects on urban heat islands. *Urban Climate, 50,* 101592. https://doi.org/10.1016/j.uclim.2023.101592

Donateo, A., Palusci, O., Pappaccogli, G., Esposito, A., Martilli, A., Santiago, J. L., & Buccolieri, R. (2023). Analysis of urban heat island and human thermal comfort in a Mediterranean city: A case study of Lecce (Italy). *Sustainable Cities and Society, 98,* 104849. https://doi.org/10.1016/j.scs.2023.104849

Kumari, P., Garg, V., Kumar, R., & Kumar, K. (2021). Impact of urban heat island formation on energy consumption in Delhi. *Urban Climate, 36,* 100763. https://doi.org/10.1016/j.uclim.2020.100763

Friederike Fachinger, Drewnick, F., & Borrmann, S. (2021). How villages contribute to their local air quality – The influence of traffic- and biomass combustion-related emissions assessed by mobile mappings of PM and its components. *Atmospheric Environment, 263,* 118648–118648. https://doi.org/10.1016/j.atmosenv.2021.118648

Abbassi, Y., Ahmadikia, H., & Baniasadi, E. (2020). Prediction of pollution dispersion under urban heat island circulation for different atmospheric stratification. *Building and Environment, 168,* 106374. https://doi.org/10.1016/j.buildenv.2019.106374

Fan, Y., Li, Y., Wang, X., & Catalano, F. (2016). A New Convective Velocity Scale for Studying Diurnal Urban Heat Island Circulation. *Journal of Applied Meteorology and Climatology, 55*(10), 2151–2164. https://doi.org/10.1175/jamc-d-16-0099.1

Yao, L., Xu, Y., Sun, S., & Wang, Y. (2022). Revisiting $PM_{2.5}$ pollution along urban-rural gradient and its coupling with urbanization process, a new perspective from urban pollution island analysis. *Urban Climate, 45,* 101270. https://doi.org/10.1016/j.uclim.2022.101270
Sun, J., Zhou, T., & Wang, D. (2022). Relationships between urban form and air quality: A reconsideration based on evidence from China's five urban agglomerations during the COVID-19 pandemic. *Land Use Policy, 118,* 106155. https://doi.org/10.1016/j.landusepol.2022.106155
Verbeek, T., & Hincks, S. (2022). The "just" management of urban air pollution? A geospatial analysis of low emission zones in Brussels and London. *Applied Geography, 140,* 102642. https://doi.org/10.1016/j.apgeog.2022.102642
Mancilla, Y., Mendoza, A., Fraser, M. P., & Herckes, P. (2016). Organic composition and source apportionment of fine aerosol at Monterrey, Mexico, based on organic markers. *Atmospheric Chemistry and Physics, 16*(2), 953–970. https://doi.org/10.5194/acp-16-953-2016
Li, Z., Xie, M., Wang, H., Chen, B., Wu, R., & Chen, Y. (2021). The spatiotemporal heterogeneity of the relationship between $PM_{2.5}$ concentrations and the surface urban heat island effect in Beijing, China. *Progress in Physical Geography, 46*(1), 84–104. https://doi.org/10.1177/03091333211033209
Feizizadeh, B., & Blaschke, T. (2013). Examining Urban Heat Island Relations to Land Use and Air Pollution: Multiple Endmember Spectral Mixture Analysis for Thermal Remote Sensing. *IEEE Journal of Selected Topics in Applied Earth Observations and Remote Sensing, 6*(3), 1749–1756. https://doi.org/10.1109/jstars.2013.2263425
Wang, Y., Guo, Z., & Han, J. (2021). The relationship between urban heat island and air pollutants and them with influencing factors in the Yangtze River Delta, China. *Ecological Indicators, 129,* 107976. https://doi.org/10.1016/j.ecolind.2021.107976
Zhong, S., Qian, Y., Sarangi, C., Zhao, C., Leung, R., Wang, H., Yan, H., Yang, T., & Yang, B. (2018). Urbanization Effect on Winter Haze in the Yangtze River Delta Region of China. *Geophysical Research Letters, 45*(13), 6710–6718. https://doi.org/10.1029/2018gl077239
Li, H., Meier, F., Lee, X., Chakraborty, T., Liu, J., Schaap, M., & Sodoudi, S. (2018). Interaction between urban heat island and urban pollution island during summer in Berlin. *Science of the Total Environment, 636,* 818–828. https://doi.org/10.1016/j.scitotenv.2018.04.254
Jiang, Y., Lin, W., Xu, D., & Xu, D. (2023). Spatio-temporal variation of the relationship between air pollutants and land surface temperature in the Yangtze River Delta Urban Agglomeration, China. *Sustainable Cities and Society,* 104429. https://doi.org/10.1016/j.scs.2023.104429
Suthar, G., Kaul, N., Khandelwal, S., & Singh, S. (2024). Dynamics of land surface temperature: Insights into vegetation, elevation, and air pollution in Bengaluru. *Remote Sensing Applications: Society and Environment, 33,* 101145. https://doi.org/10.1016/j.rsase.2024.101145
Arunab, K. S., & Mathew, A. (2024). Quantifying urban heat island and pollutant nexus: A novel geospatial approach. *Sustainable Cities and Society, 101,* 105117. https://doi.org/10.1016/j.scs.2023.105117
Cao, W., Zhou, W., Yu, W., & Wu, T. (2024). Combined effects of urban forests on land surface temperature and $PM_{2.5}$ pollution in the winter and summer. *Sustainable Cities and Society, 104,* 105309. https://doi.org/10.1016/j.scs.2024.105309
Lei, Y., Davies, G. M., Jin, H., Tian, G., & Kim, G. (2021). Scale-dependent effects of urban greenspace on particulate matter air pollution. *Urban Forestry & Urban Greening, 61,* 127089. https://doi.org/10.1016/j.ufug.2021.127089
Wu, H., Yang, C., Chen, J., Yang, S., Lu, T., & Lin, X. (2018). Effects of Green space landscape patterns on particulate matter in Zhejiang Province, China. *Atmospheric Pollution Research, 9*(5), 923–933. https://doi.org/10.1016/j.apr.2018.03.004
Wei, J., Li, Z., Lyapustin, A., Sun, L., Peng, Y., Xue, W., Su, T., & Cribb, M. (2021). Reconstructing 1-km-resolution high-quality $PM_{2.5}$ data records from 2000 to 2018 in China: spatiotemporal variations and policy implications. *Remote Sensing of Environment, 252,* 112136. https://doi.org/10.1016/j.rse.2020.112136
Wei, J., Li, Z., Cribb, M., Huang, W., Xue, W., Sun, L., Guo, J., Peng, Y., Li, J., Lyapustin, A., Liu, L., Wu, H., & Song, Y. (2020). Improved 1 km resolution $PM_{2.5}$ estimates across China using enhanced space–time extremely randomized trees. *Atmospheric Chemistry and Physics, 20*(6), 3273–3289. https://doi.org/10.5194/acp-20-3273-2020
Yang, J., & Huang, X. (2022). The 30 m annual land cover datasets and its dynamics in China from 1990 to 2021. *Zenodo (CERN European Organization for Nuclear Research)*. https://doi.org/10.5281/zenodo.5816591
Rey, S. J., & Janikas, M. V. (2009). STARS: Space-Time Analysis of Regional Systems. *Springer EBooks,* 91–112. https://doi.org/10.1007/978-3-642-03647-7_6
Rey, S. J. (2010). *Spatial Empirics for Economic Growth and Convergence. Geographical Analysis, 33*(3), 195–214. https://doi.org/10.1111/j.1538-4632.2001.tb00444.x
Wang, Z., & Cheng, Z. H. (2023). Spatiotemporal interaction characteristics and transition mechanism of carbon intensity in China's service industry under the targets of carbon peak and carbon neutrality. *Acta Geographica Sinica, 78*(1), 54 - 70. https://doi.org/10.11821/dlxb202301004
Zhou, W.-X. (2008). *Multifractal detrended cross-correlation analysis for two nonstationary signals. Physical Review E, 77*(6). https://doi.org/10.1103/physreve.77.066211
Li, Y., Fan, B., Deng, G., Zhang, H., Zhang, J., Du, H., & Shi, K. (2024). Effect of NO2 on SO2-SO42- conversion in atmosphere: Evidence from long-term precipitation. *Atmospheric Environment, 334,* 120707–120707. https://doi.org/10.1016/j.atmosenv.2024.120707
Ma, D., Zhang, J., An, B., Guo, Z., Zhang, F., Yan, Y., & Peng, G. (2024). Research on urban land green use efficiency and influencing factors based on DEA and ESTDA models: Taking 284 cities in China as an example. *Ecological Indicators, 160,* 111824–111824. https://doi.org/10.1016/j.ecolind.2024.111824
Zhang, J., Yang, F., Duan, N., Zheng, B., Xiong, S., & Xu, Y. (2024). Spatial transition and obstacle factor diagnosis based on the evaluation of the quality of arable land use in plain Lake Areas: A case study of the Dongting Lake region. Ecological Indicators, 169, 112881–112881. https://doi.org/10.1016/j.ecolind.2024.112881
Xiang, S., Huang, X., Lin, N., & Yi, Z. (2025). Synergistic reduction of air pollutants and carbon emissions in Chengdu-Chongqing urban agglomeration, China: Spatial-temporal characteristics, regional differences, and dynamic evolution. Journal of Cleaner Production, 144929–144929. https://doi.org/10.1016/j.jclepro.2025.144929